

Spin-valley locking in Kekulé-distorted graphene with Dirac-Rashba interactions

David A. Ruiz-Tijerina,^{1,*} Jesús Arturo Sánchez-Sánchez,^{2,3} Ramon Carrillo-Bastos,⁴ Santiago Galván y García,^{2,3} and Francisco Mireles^{2,†}

¹*Departamento de Física Química, Instituto de Física, Universidad Nacional Autónoma de México, Ciudad de México, C.P. 04510, México*

²*Departamento de Física, Centro de Nanociencias y Nanotecnología,*

Universidad Nacional Autónoma de México, Apdo. Postal 14, 22800 Ensenada, Baja California, México

³*Instituto de Ciencias Físicas, Universidad Nacional Autónoma de México, Cuernavaca, Morelos, 62210, México*

⁴*Facultad de Ciencias, Universidad Autónoma de Baja California, Apdo. Postal 1880, 22800 Ensenada, Baja California, México.*

(Dated: August 7, 2023)

The joint effects of Kekulé lattice distortions and Rashba-type spin-orbit coupling on the electronic properties of graphene are explored. We modeled the position dependence of the Rashba energy term in a manner that allows its seamless integration into the scheme introduced by Gamayun *et al.*[1] to describe graphene with Kekulé lattice distortion. Particularly for the Kekulé-Y texture, the effective low energy Dirac Hamiltonian contains a new spin-valley locking term, in addition to the well-known Rashba-induced momentum-pseudospin and spin-pseudospin couplings, and the Kekulé-induced momentum-valley coupling term. We report on the low-energy band structure and Landau level spectra of Rashba-spin-orbit-coupled Kek-Y graphene, and propose an experimental scheme to discern between the presence of Rashba spin-orbit coupling, Kek-Y lattice distortion, and both, based on doping-dependent magnetotransport measurements.

I. INTRODUCTION

In recent years, graphene-metal hybrid systems have attracted much attention because they showcase new and exciting electronic and magnetic phenomena not present in pristine graphene [2]. Through proximity effects, these hybrid systems enable the modification and control of the electronic properties of pristine graphene, such as opening a gap between the valence and conduction bands[3]; distorting the linear behavior of carriers at low energies[4]; and introducing the anomalous, spin and spin-quantum Hall effects[5–7]. Researchers aim to break graphene’s symmetries—from which many of its extraordinary properties originate—through various mechanisms, to turn graphene into a suitable candidate for spintronic applications [8]. Two of the most actively researched mechanisms for breaking graphene’s symmetries are lattice deformations, and spin-orbit effects induced by proximity[9–13]. Throughout this paper, we shall focus on these two mechanisms, combining specifically Kekulé lattice distortions, and proximity-induced Rashba spin-orbit (RSO) coupling.

On the one hand, a Kekulé Y-shaped bond pattern (Kek-Y) was experimentally obtained in 2016 by Gutierrez *et al.*[14, 15] by growing graphene epitaxially on a Cu(111) surface, and attributed to the commensurate lattice constants of graphene and the copper substrate, combined with the presence of copper vacancies acting as “ghost” adatoms. Eom and Koo[16] observed both Kek-Y and Kek-O textures by inducing nanoscale strain

on graphene using a silicon dioxide substrate. Finally, the graphene Kek-O texture has been observed by Li *et al.* in quantum Hall ferromagnetic states[17], and more recently by Bao *et al.* in Li-intercalated graphene samples[18, 19], and by Qu *et al.* in graphene decorated with Li adatoms[20]. In order to determine the electronic structure of graphene with Kekulé lattice distortion, Gamayun *et al.*[1] derived low-energy Dirac Hamiltonians for both the Kek-Y and Kek-O textures. In the former case, they found that the lattice distortion introduces a new coupling between the electronic momentum and its valley isospin, as a result of the broken chiral symmetry. The low-energy spectrum preserved its linear behavior near the Fermi level, but with the valley degeneracy breaking resulting in two Dirac bands with distinct Fermi velocities.

On the other hand, a Rashba-type spin-orbit coupling has been confirmed in graphene due to proximity effects with metallic substrates. This extrinsic effect is momentum independent in the single valley approximation, and causes an energy splitting between opposite spin states of 13 – 225 meV [21–24]: three to four orders of magnitude greater than the splitting associated with graphene’s intrinsic spin-orbit coupling[25, 26]. Such a substantial enhancement of the RSO interaction has been mainly attributed to hybridization between carbon’s $2p_z$ orbitals and the metal substrate’s d orbitals, and broken lattice symmetry in graphene[27]. Moreover, the RSO interaction strength has been shown to be tunable via external gate voltages, as well as local lattice deformations[11, 28].

Given the bond length dependency of the Rashba parameter[28], the following question naturally arises: How will the RSO coupling be modified by the presence of Kekulé lattice distortions in graphene? In this paper, we aim to answer this question. We introduce a gener-

* d.ruiz-tijerina@fisica.unam.mx

† fmireles@ens.cnyn.unam.mx

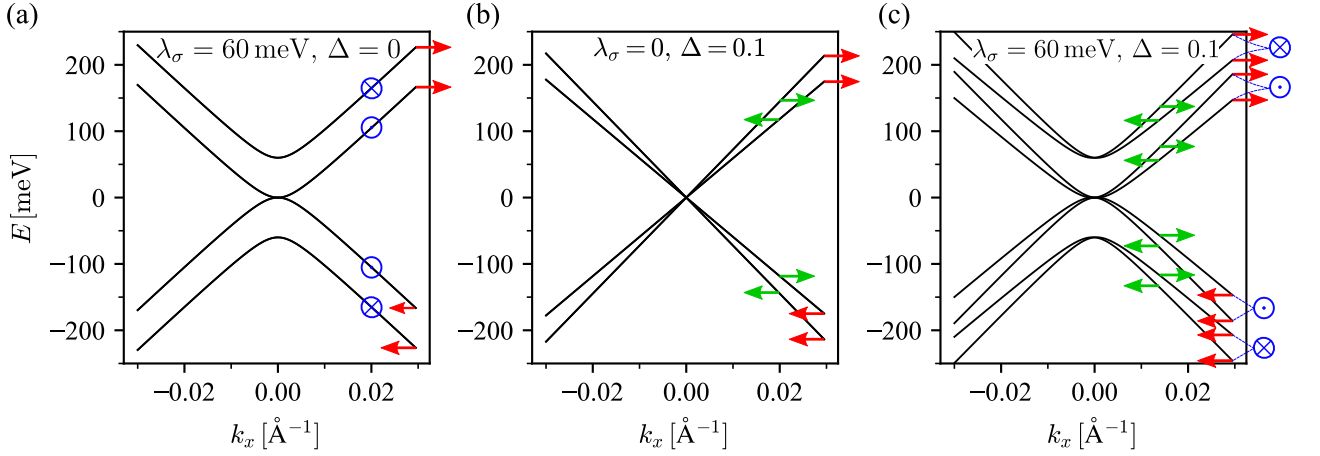


FIG. 1. Band structure (19a) for Kek-Y graphene, for parameters (a) $\lambda_\sigma \neq 0$ and $\Delta = 0$; (b) $\lambda_\sigma = 0$ and $\Delta \neq 0$; and (c) $\lambda_\sigma \neq 0$ and $\Delta \neq 0$. In all cases, the Kekulé-induced modulation to the RSO coupling was set to $\xi = 0$. Blue, red and green arrows indicate the spin, sublattice and valley polarizations, respectively, with \otimes and \odot representing arrows pointing in the negative and positive \hat{z} directions, respectively.

alized tight-binding Hamiltonian for graphene with RSO coupling and Kekulé lattice distortion, parameterized via position-dependent hopping- and spin-orbit interaction terms, exhibiting the Kekulé periodicity. After mapping the problem onto reciprocal space and folding the graphene bands onto the Kekulé Brillouin zone (KBZ), we derive effective $\mathbf{k} \cdot \mathbf{p}$ -type Hamiltonians for both the Kek-Y and Kek-O textures, valid for the bands nearest the Fermi level. We then use these effective Hamiltonians to compute the low-energy band spectra of Kekulé distorted graphene with RSO coupling, and discuss its most salient features, including the resulting spin, pseudospin and valley textures. Finally, we introduce an out-of-plane magnetic field in the minimal coupling approximation[29] for the Kek-Y case, and compute its Landau level (LL) spectrum, focusing on the competing effects of the Kekulé and RSO terms in magnetotransport. In particular, we identify different trends for the horizontal LL splittings in a carrier density vs. magnetic field diagram, in the cases of graphene with only a Kek-Y distortion, graphene with only RSO coupling, and graphene with both a Kek-Y distortion and RSO coupling. We propose that these distinct trends may be used to experimentally identify the presence of Kek-Y distortions, RSO coupling, or both, on graphene-metal hybrid structures.

II. TIGHT-BINDING MODEL

A. Tight-binding model

The tight-binding Hamiltonian for a single layer of graphene with proximity-induced, sublattice-resolved Dirac-Rashba spin-orbit coupling[30, 31], and a Kekulé lattice distortion[1], can be written as $H^{pq} = H_0^{pq} + H_R^{pq}$,

with the spinless graphene Hamiltonian

$$H_0^{pq} = - \sum_{\mu} \sum_{\mathbf{R}} \sum_{j=1}^3 \left(t_{\mathbf{R}, \mathbf{R}+\delta_j}^{pq} a_{\mathbf{R}, \mu}^\dagger b_{\mathbf{R}+\delta_j, \mu} + \text{H.c.} \right), \quad (1)$$

where $a_{\mathbf{R}, \mu}^\dagger$ ($a_{\mathbf{R}, \mu}$) is the creation (annihilation) operator for an electron on site \mathbf{R} of sublattice A , with spin projection $\mu = \uparrow, \downarrow$, and $b_{\mathbf{R}+\delta_j, \mu}^\dagger$ ($b_{\mathbf{R}+\delta_j, \mu}$) are the corresponding B sublattice operators. The integers p, q parametrize the Kekulé bond texture over the honeycomb lattice, as shown below [see Eqs. (2) and (7)]. In the case of pristine graphene ($\Delta = 0$), each atom at site \mathbf{R} is connected with three nearest neighbors at sites $\mathbf{R} + \delta_j$, with relative position vectors $\delta_1 = \frac{a_0}{2}(\sqrt{3}, -1)$, $\delta_2 = -\frac{a_0}{2}(\sqrt{3}, 1)$ and $\delta_3 = a_0(0, 1)$, where $a_0 = 1.421 \text{ \AA}$ is the unperturbed C-C bond length. The lattice vectors are $\mathbf{a}_1 = \delta_3 - \delta_1$ and $\mathbf{a}_2 = \delta_3 - \delta_2$. However, the presence of a Kekulé bond distortion will modulate the hopping terms $t_{\mathbf{R}, \mathbf{R}+\delta_j}^{pq}$ as[1]

$$\frac{t_{\mathbf{R}, \mathbf{R}+\delta_j}^{pq}}{t_0} = 1 + 2\text{Re} \left[\Delta e^{i\mathbf{K}_{pq} \cdot \delta_j + i\mathbf{G} \cdot \mathbf{R}} \right]. \quad (2)$$

Here, $\mathbf{K}_{pq} \equiv p\mathbf{K}_+ + q\mathbf{K}_-$, with the graphene valley vectors

$$\mathbf{K}_\pm = \frac{4\pi}{3\sqrt{3}a_0} \left(\pm \frac{1}{2}, \frac{\sqrt{3}}{2} \right), \quad (3)$$

and the vector

$$\mathbf{G} \equiv \mathbf{K}_+ - \mathbf{K}_- = \frac{4\pi}{3\sqrt{3}a_0} (1, 0) \quad (4)$$

is a Kekulé superlattice primitive Bragg vector. The type of bond texture is determined by the integer ($\in \mathbb{Z}_3$)

$$n = (1 + q - p) \bmod 3, \quad (5)$$

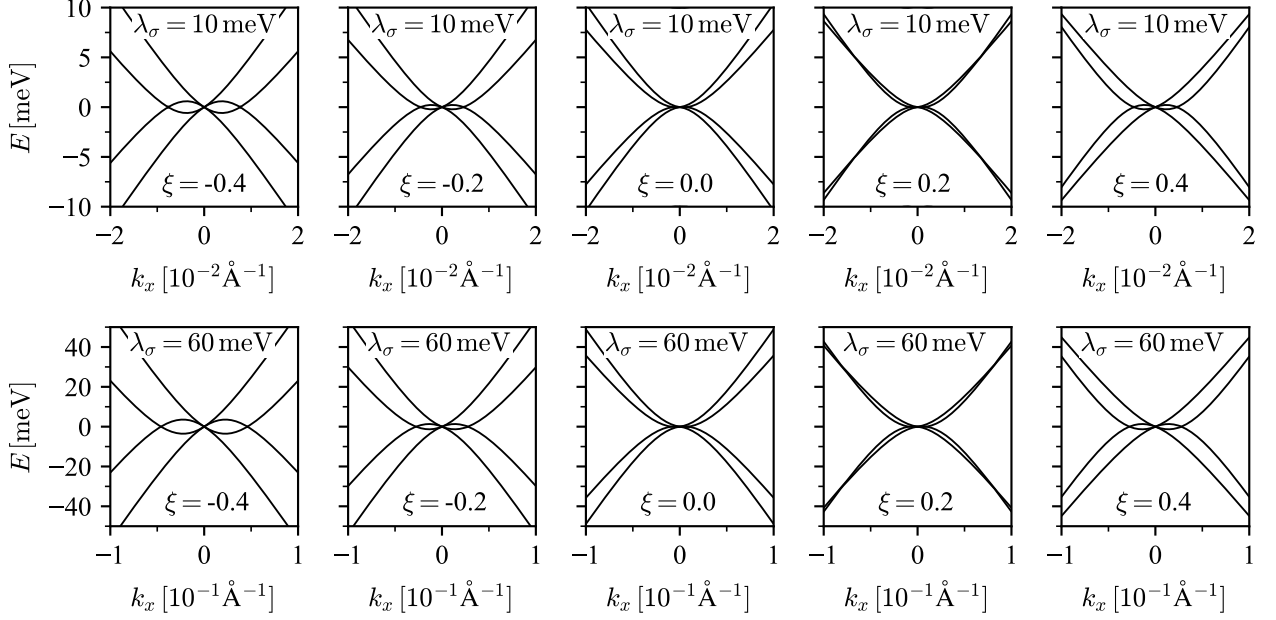


FIG. 2. Low energy bands of Kek-Y graphene for different values of the Kekulé-induced RSO modulation ξ , for fixed $\Delta = 0.1$, and $\lambda_\sigma = 10$ meV (top row) and $\lambda_\sigma = 60$ meV (bottom row). Note the qualitative similarities between the two cases when both axes are appropriately rescaled.

where a Kek-O texture corresponds to $n = 0$, whereas Kek-Y textures are obtained for $n = \pm 1$.

Since \mathbf{G} connects the two graphene valleys \mathbf{K}_\pm in reciprocal space, the latter are folded down onto the Γ -point of the KBZ. The hopping term modulation amplitude Δ is, in general, complex valued, although in the remainder of this paper we shall take both Δ and t as real, without loss of generality. Finally, we point out that, for pristine graphene, the nearest-neighbor hopping integral reduces to $t_0 = 3.16$ eV.

The Dirac-Rashba spin-orbit term has the form

$$H_R^{pq} = \sum_{\mu\nu} \sum_{\mathbf{R}} \sum_{j=1}^3 \left[\frac{i\lambda_{\mathbf{R},\mathbf{R}+\delta_j}^{pq}}{2} a_{\mathbf{R},\mu}^\dagger (\mathbf{s}_{\mu\nu} \times \hat{\delta}_j)_z b_{\mathbf{R}+\delta_j,\nu} - \text{H.c.} \right], \quad (6)$$

where \mathbf{s} is the vector of Pauli matrices acting on the phys-

ical spin subspace, whereas $\hat{\delta}_j = \delta_j/|\delta_j|$. We have allowed a periodic bond-length modulation of the Rashba spin-orbit coupling $\lambda_{\mathbf{R},\mathbf{R}+\delta_j}^{pq}$, analogous to that of the hopping parameter in Eq. (2), with a complex amplitude ξ :

$$\frac{\lambda_{\mathbf{R},\mathbf{R}+\delta_j}^{pq}}{\lambda_R} = 1 + 2\text{Re} \left[\xi e^{i\mathbf{K}_{pq} \cdot \delta_j + i\mathbf{G} \cdot \mathbf{R}} \right], \quad (7)$$

where λ_R is the Dirac-Rashba parameter in the absence of a Kekulé distortion.

B. Total Hamiltonian in reciprocal space

Taking the Fourier transforms of the total Hamiltonian gives the spin-conserving and Dirac-Rashba terms as

$$\begin{aligned} H_0^{pq} &= \sum_{\mathbf{k} \in \text{BZ}} \sum_{\mu} \left[\Phi(\mathbf{k}) a_{\mathbf{k},\mu}^\dagger b_{\mathbf{k},\mu} + \Delta \Phi(\mathbf{k} + \mathbf{K}_{pq}) a_{\mathbf{k}+\mathbf{G},\mu}^\dagger b_{\mathbf{k},\mu} + \Delta \Phi(\mathbf{k} - \mathbf{K}_{pq}) a_{\mathbf{k}-\mathbf{G},\mu}^\dagger b_{\mathbf{k},\mu} + \text{H.c.} \right], \\ H_R^{pq} &= i \sum_{\mathbf{k} \in \text{BZ}} \sum_{\mu,\nu} \left[a_{\mathbf{k},\mu}^\dagger \Lambda_{\mu\nu}(\mathbf{k}) b_{\mathbf{k},\nu} + \xi a_{\mathbf{k}+\mathbf{G},\mu}^\dagger \Lambda_{\mu\nu}(\mathbf{k} + \mathbf{K}_{pq}) b_{\mathbf{k},\nu} + \xi a_{\mathbf{k}-\mathbf{G},\mu}^\dagger \Lambda_{\mu\nu}(\mathbf{k} - \mathbf{K}_{pq}) b_{\mathbf{k},\nu} - \text{H.c.} \right], \end{aligned} \quad (8)$$

with the sum over \mathbf{k} running over all wave vectors of the original (pristine graphene) Brillouin zone (BZ). We have also defined

$$\Phi(\mathbf{k}) = -t_0 \sum_{j=1}^3 e^{i\mathbf{k} \cdot \delta_j}, \quad \Lambda_{\mu\nu}(\mathbf{k}) = \frac{\lambda_R}{2} \sum_{j=1}^3 e^{i\mathbf{k} \cdot \delta_j} (\mathbf{s}_{\mu\nu} \times \hat{\delta}_j)_z. \quad (9)$$

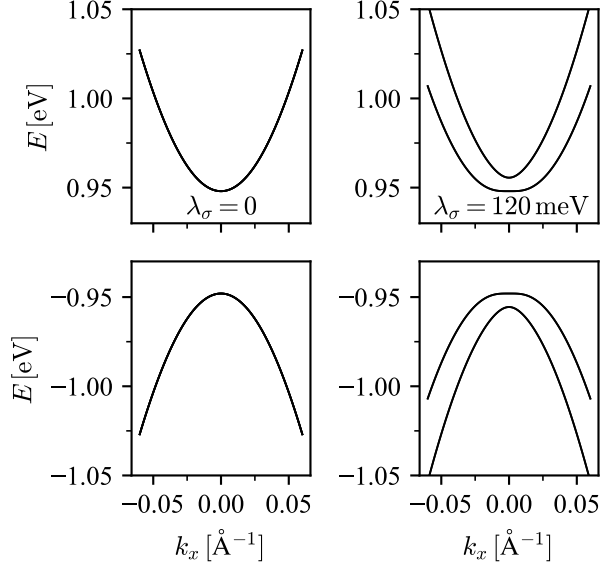


FIG. 3. Band structures of the Hamiltonian (18) for Kek-O graphene, for RSO coupling $\lambda_\sigma = 0$ and 120 meV, for fixed $\Delta = 0.1$.

We now perform a zone folding from the original BZ onto the KBZ by introducing the 12-spinors $\Psi_{\mathbf{k}} = (c_{\mathbf{k},\uparrow}, c_{\mathbf{k},\downarrow})^T$, where

$$c_{\mathbf{k},\mu} = (a_{\mathbf{k},\mu}, a_{\mathbf{k}-\mathbf{G},\mu}, a_{\mathbf{k}+\mathbf{G},\mu}, b_{\mathbf{k}-\mathbf{G},\mu}, b_{\mathbf{k}+\mathbf{G},\mu}, b_{\mathbf{k},\mu})^T, \quad (10)$$

and $\mathbf{k} \in \text{KBZ}$. Using the properties ($m \in \mathbb{Z}$)

$$\Xi(\mathbf{k}) = e^{i\frac{2\pi}{3}m} \Xi(\mathbf{k} + m(\mathbf{K}_+ + \mathbf{K}_-)) = \Xi(\mathbf{k} + 3m\mathbf{K}_\pm), \quad (11)$$

valid for both $\Xi(\mathbf{k}) = \Phi(\mathbf{k})$ and $\Xi(\mathbf{k}) = \Lambda(\mathbf{k})$, we may write

$$H^{pq} = \sum_{\mathbf{k} \in \text{KBZ}} \Psi_{\mathbf{k}}^\dagger \mathcal{H}_{pq}(\mathbf{k}) \Psi_{\mathbf{k}}, \quad (12)$$

with the Bloch Hamiltonian

$$\mathcal{H}_{pq}(\mathbf{k}) = \begin{pmatrix} 0 & \mathcal{E}_n(\mathbf{k}) & 0 & i\mathcal{R}_n^{\uparrow\downarrow}(\mathbf{k}) \\ \mathcal{E}_n^\dagger(\mathbf{k}) & 0 & -i\mathcal{R}_n^{\downarrow\uparrow*}(\mathbf{k}) & 0 \\ 0 & i\mathcal{R}_n^{\downarrow\uparrow}(\mathbf{k}) & 0 & \mathcal{E}_n(\mathbf{k}) \\ -i\mathcal{R}_n^{\uparrow\downarrow*}(\mathbf{k}) & 0 & \mathcal{E}_n^\dagger(\mathbf{k}) & 0 \end{pmatrix} \quad (13)$$

containing the matrices

$$\mathcal{E}_n(\mathbf{k}) = \begin{pmatrix} \Phi_0(\mathbf{k}) & \Delta_{pq}\Phi_{n+1}(\mathbf{k}) & \Delta_{pq}^*\Phi_{-n-1}(\mathbf{k}) \\ \Delta_{pq}^*\Phi_{-n+1}(\mathbf{k}) & \Phi_{-1}(\mathbf{k}) & \Delta_{pq}\Phi_n(\mathbf{k}) \\ \Delta_{pq}\Phi_{n-1}(\mathbf{k}) & \Delta_{pq}^*\Phi_{-n}(\mathbf{k}) & \Phi_1(\mathbf{k}) \end{pmatrix},$$

$$\mathcal{R}_n^{\mu\nu}(\mathbf{k}) = \begin{pmatrix} \Lambda_0^{\mu\nu}(\mathbf{k}) & \xi_{pq}\Lambda_{n+1}^{\mu\nu}(\mathbf{k}) & \xi_{pq}^*\Lambda_{-n-1}^{\mu\nu}(\mathbf{k}) \\ \xi_{pq}^*\Lambda_{-n+1}^{\mu\nu}(\mathbf{k}) & \Lambda_{-1}^{\mu\nu}(\mathbf{k}) & \xi_{pq}\Lambda_n^{\mu\nu}(\mathbf{k}) \\ \xi_{pq}\Lambda_{n-1}^{\mu\nu}(\mathbf{k}) & \xi_{pq}^*\Lambda_{-n}^{\mu\nu}(\mathbf{k}) & \Lambda_1^{\mu\nu}(\mathbf{k}) \end{pmatrix}, \quad (14)$$

where we have introduced the folded tunneling function $\Phi_n(\mathbf{k}) \equiv \Phi(\mathbf{k} + n\mathbf{G})$ and RSO coupling $\Lambda_n^{\mu\nu}(\mathbf{k}) \equiv \Lambda_{\mu\nu}(\mathbf{k} + n\mathbf{G})$, with n given by Eq. (5). We have also introduced the the Kekulé terms

$$\Delta_{pq} \equiv e^{i\frac{2\pi}{3}(p+q)}\Delta, \quad \xi_{pq} \equiv e^{i\frac{2\pi}{3}(p+q)}\xi. \quad (15)$$

Note that all terms $\Lambda_{\uparrow\uparrow}(\mathbf{k} + n\mathbf{G}) = \Lambda_{\downarrow\downarrow}(\mathbf{k} + n\mathbf{G}) = 0$, by the symmetry of the Pauli matrices.

We may now obtain an effective low-energy model with reduced dimensionality 8×8 by projecting out the two high-energy electron- and hole bands present in $\mathcal{H}_{pq}(\mathbf{k})$ for \mathbf{k} near the Γ point, corresponding to operators $a_{\mathbf{k},\mu}$ and $b_{\mathbf{k},\mu}$ in Eq. (10). We do so at zeroth order in perturbation theory, and linearize $\Phi_n(\mathbf{k})$ and $\Lambda_n(\mathbf{k})$ about $\mathbf{k} = \mathbf{0}$. Finally, introducing the new 8-spinor basis

$$\Psi'_{\mathbf{k}} = (-b_{\mathbf{k}-\mathbf{G}\uparrow}, -b_{\mathbf{k}-\mathbf{G}\downarrow}, a_{\mathbf{k}-\mathbf{G}\uparrow}, a_{\mathbf{k}-\mathbf{G}\downarrow}, a_{\mathbf{k}+\mathbf{G}\uparrow}, a_{\mathbf{k}+\mathbf{G}\downarrow}, b_{\mathbf{k}+\mathbf{G}\uparrow}, b_{\mathbf{k}+\mathbf{G}\downarrow})^T, \quad (16)$$

we obtain two compact forms of $\tilde{\mathcal{H}}_{pq}$ (Appendix A): all cases when $(1+q-p) \bmod 3 = \pm 1$ give the Kek-Y Bloch Hamiltonians

$$\mathcal{H}_Y(\mathbf{k}) = \hbar v_\sigma \tau_0 (\mathbf{k} \cdot \boldsymbol{\sigma}) s_0 + \frac{\lambda_\sigma}{2} \tau_0 (\boldsymbol{\sigma} \times \mathbf{s})_z + \hbar v_\tau (\mathbf{k} \cdot \boldsymbol{\tau}_\pm) \sigma_0 s_0 + \frac{\lambda_\tau}{2} (\boldsymbol{\tau}_\pm \times \sigma_0 \mathbf{s})_z, \quad (17)$$

whereas for $(1+q-p) \bmod 3 = 0$ we obtain the Kek-O model

$$\mathcal{H}_O(\mathbf{k}) = \hbar v_\sigma \tau_0 (\mathbf{k} \cdot \boldsymbol{\sigma}) s_0 + \frac{\lambda_\sigma}{2} \tau_0 (\boldsymbol{\sigma} \times \mathbf{s})_z + 3t_0 \Delta \tau_x \sigma_z s_0. \quad (18)$$

Here, we have used the standard definitions of the Pauli matrix vectors $\boldsymbol{\sigma}$ and \mathbf{s} acting on the sublattice and spin degrees of freedom, respectively. For the valley subspace, we have defined the Pauli vectors $\boldsymbol{\tau}_n = (n\tau_x, \tau_y, \tau_z)$, where $n = \pm 1$ corresponds to the type of Kek-Y texture defined by the parameters p and q . τ_0 , σ_0 and s_0 are the unit matrices in the valley, sublattice and spin subspaces. We have also defined the two Fermi velocities $v_\sigma = \frac{3}{2\hbar} t_0 a_0$ and $v_\tau = \Delta v_\sigma$, and the constants $\lambda_\sigma = \frac{3}{2} \lambda_R$ and $\lambda_\tau = \xi \lambda_\sigma$. The latter, introduced by the Kekulé-modulated RSO interaction in the Kek-Y case, constitutes a novel spin-valley coupling. By contrast, note that in a Kek-O texture there is no coupling between valley and momentum, or valley and spin.

Both models \mathcal{H}_Y and \mathcal{H}_O can be diagonalized exactly, yielding the band structures

$$E_{\alpha,\beta,\gamma}^Y(\mathbf{k}) = \frac{\alpha}{2} \left[\sqrt{(2\hbar v_\tau k + \beta\gamma\lambda_\sigma)^2 + \lambda_\tau^2} + \gamma \sqrt{(2\hbar v_\sigma k + \beta\gamma\lambda_\tau)^2 + \lambda_\sigma^2} \right], \quad (19a)$$

$$E_{\alpha,\beta}^O(\mathbf{k}) = \alpha \left[(\hbar v_\sigma k)^2 + (3t_0\Delta)^2 + \frac{\lambda_\sigma^2}{8} + \beta\lambda_\sigma \sqrt{(\hbar v_\sigma k)^2 + \left(\frac{\lambda_\sigma}{2}\right)^2} \right]^{1/2}, \quad (19b)$$

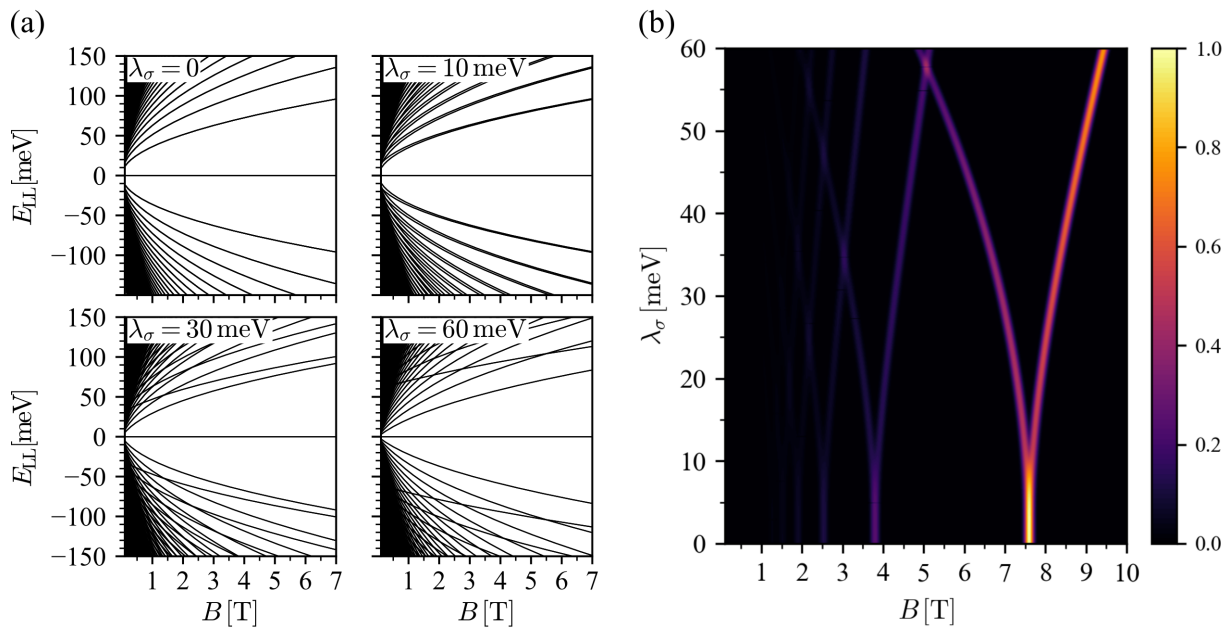


FIG. 4. (a) Landau levels for different values of λ_σ , and (b) $B^2 \cdot \text{DOS}(\epsilon_F)$ (arbitrary units) as a function of λ_σ and magnetic field, for $\Delta = \xi = 0$. In panel (b) we have set $\epsilon_F = 50$ meV.

where the indices $\alpha, \beta, \gamma = \pm 1$. Note that in the Kek-Y case, the dispersions are identical for $n = \pm 1$. Figure 1 shows the band structure (19a) along the $-\overline{M}\Gamma\overline{M}$ line ($k_y = 0$) of the KBZ, for different values of the RSO coupling λ_σ and Kekulé hopping modulation Δ , keeping the Rashba modulation parameter $\xi = 0$. Setting $\Delta = 0$ for finite λ_σ , we obtain the well known band structure of RSO-coupled graphene[21, 32], except folded onto the KBZ, leading to a double degeneracy for each band, corresponding to the valley pseudo-spin. Figure 1(a) also shows the expectation values of the s and σ operators as blue and red arrows, respectively, showing that the sublattice polarization for all bands is locked perpendicularly to the spin, forming a right-handed (left-handed) pair for the first conduction and second valence (second conduction and first valence) bands, with the sublattice (spin) vector always pointing in the radial (polar) direction.

Figure 1(b) shows the case of $\lambda_\sigma = 0$ with a finite Kekulé hopping modulation Δ , reproducing the band structure of ordinary Kek-Y graphene[1], consisting of two concentric Dirac cones with different Fermi velocities, $v_\sigma \pm v_\tau$. All bands are spin degenerate and valley-sublattice locked into parallel (second conduction- and valence bands) or anti-parallel (first conduction- and valence bands) pairs, with both vectors always oriented radially. This is shown in Fig. 1(b), where the sublattice and valley vectors are shown with red and green arrows, respectively.

Next, Fig. 1(c) shows the band structure for Kek-Y graphene ($\Delta \neq 0$) with a finite RSO coupling ($\lambda_\sigma \neq 0$). As in the case of ordinary Kek-Y graphene, each band has radial valley and sublattice polarizations, locked into parallel or anti-parallel pairs. Moreover, for each band

the spin orientation is also locked with the sublattice vector, forming either left- or right-handed pairs. All band structures in Fig. 1 are particle-hole symmetric, as a consequence of the chiral symmetry $\{\mathcal{H}_Y(\mathbf{k}), \tau_z \sigma_z s_0\} = 0$, which is exact for all parameter values. This chirality operator was first identified by Gamayun *et al.*[1] for ordinary Kek-Y graphene ($\lambda_\sigma = 0$).

Finally, Fig. 2 shows how the Kekulé-induced modulation to the RSO coupling ξ modifies the band structure of Kek-Y graphene, focusing on the first two conduction- and valence bands, and choosing large values $|\xi| = 0.2, 0.4$ to clearly see its effects on the band structure. For either positive or negative ξ , Fig. 2 reveals the appearance of a doubly degenerate Dirac cone centered at the Γ point, surrounded by a circular band touching at the Fermi level centered at the Γ point, with bands that disperse linearly in the radial direction away from the touching points. The resulting Fermi surface is a nondegenerate circle surrounding a doubly degenerate point at Γ . The radius of the Fermi circle increases with $|\xi|$, and the case $\xi = 0$ represents a critical point where the Fermi surface becomes a quadruply degenerate point at Γ .

For completeness, Fig. 3 shows the band structures of Kek-O graphene for $\lambda_\sigma = 0$ and 60 meV, and fixed $\Delta = 0.1$. It exhibits a large, direct band gap of size $6t_0\Delta \approx 1.9$ eV at the Γ point, coming from the valley-sublattice coupling in Eq. (18). For $\lambda_\sigma = 0$, the conduction and valence bands are parabolic, whereas for finite λ we obtain the typical band structure of RSO-coupled parabolic bands. Note that the Kekulé-induced Rashba modulation ξ does not appear in the Kek-O Hamiltonian (18). Henceforth, we shall focus on the Kek-Y case, which we deem more interesting due to

its lack of a band gap and the chiral nature of its bands.

III. LANDAU LEVEL SPECTRUM OF KEK-Y GRAPHENE WITH RSO COUPLING

We introduce an out-of-plane magnetic field $\mathbf{B} = B\hat{z}$, with symmetric-gauge vector potential $\mathbf{A} = \frac{B}{2}(-y\hat{x} + x\hat{y})$, into the Kek-Y graphene Hamiltonian (17)[33], via the minimal substitution $\hbar\mathbf{k} \rightarrow \hbar\mathbf{k} - \frac{e}{c}\mathbf{A} = \boldsymbol{\pi}$, where the components of the canonical momentum $\boldsymbol{\pi}$ obey the algebra $[\pi_x, \pi_y] = -i\frac{e}{c}\hbar B$. This allows the introduction of the ladder operators ($\pi_{\pm} \equiv \pi_x \pm i\pi_y$)

$$a = \sqrt{\frac{c}{2e\hbar B}}\pi_-, \quad a^\dagger = \sqrt{\frac{c}{2e\hbar B}}\pi_+, \quad (20)$$

obeying the harmonic oscillator algebra $[a, a^\dagger] = 1$, and operating on the Landau level (LL) basis $\{|\ell\rangle\}$ as $a|\ell\rangle = \sqrt{\ell}|\ell-1\rangle$ and $a^\dagger|\ell\rangle = \sqrt{\ell+1}|\ell+1\rangle$, for integer $\ell \geq 0$. These operators enter the Kek-Y Hamiltonian (17) through the substitution

$$\boldsymbol{\pi} \cdot \boldsymbol{\nu} = \pi_+\nu_- + \pi_-\nu_+ = \sqrt{\frac{2e\hbar B}{c}}(a^\dagger\nu_- + a\nu_+), \quad (21)$$

where $\boldsymbol{\nu} = \boldsymbol{\tau}, \boldsymbol{\sigma}$. The resulting LL Hamiltonian is shown in its full form in Appendix B. Here, we merely report its numerical energy spectra for varying magnetic field.

Figure 4(a) shows the LLs obtained in the absence of a Kek-Y deformation, for multiple values of the RSO coupling λ_σ , including $\lambda_\sigma = 0$, which corresponds to the case of pristine graphene. In that case [34], a four-fold degenerate zero energy mode appears for all magnetic field values, surrounded by an electron-hole symmetric fan of valley- and spin-degenerate LLs evolving as $B^{1/2}$. The zero modes persist for finite λ_σ , and the surrounding LLs split into two distinct fans, corresponding to the two separate conduction- and valence bands shown in Fig. 1(a). As a connection with transport experiments, Fig. 4(b) shows the density of states (DOS) at the Fermi level as a function of both magnetic field and λ_σ , setting $\varepsilon_F = 50$ meV.

Next, Fig. 5 shows the LL spectrum of Kek-Y graphene for multiple values of Δ , setting $\lambda_\sigma = \xi = 0$, showing that the zero-mode quadruplet also survives in the presence of the Kekulé deformation, as reported in Ref. 1. The reference LL fan of pristine graphene splits into two separate fans when $\Delta \neq 0$. Note, however, that this splitting occurs only at finite magnetic fields, and both fans evolve with magnetic field as $B^{1/2}$, by contrast to the case of Rashba-SO-coupled graphene. This is a consequence of the two Dirac cones with different Fermi velocities v_σ and v_τ , shown in Fig. 1(b). Figure 5(b) shows the Fermi-level DOS for $\varepsilon_F = 50$ meV, as it evolves with the Kekulé hopping modulation Δ . Importantly, we can see that the DOS peaks split with increasing Δ , analogously to the case of RSO coupling shown in Fig. 4(b). In other words,

a splitting in the DOS peaks, measured in magnetotransport experiments as split conductance peaks, may come from either source. However, as we discuss next, the two effects can be distinguished through doping dependent transport measurements. For completeness, the LL spectrum of graphene with both a Kek-Y distortion and RSO coupling is shown in Appendix C.

Figure 6 shows the DOS at the Fermi level for varying magnetic field B and Fermi energy ε_F , keeping the model parameters in (17) constant, with $\xi = 0$ in all cases. Qualitatively similar behaviors are observed both for finite λ_σ and no Kek-Y distortion (left panels) and for no RSO coupling with finite Kek-Y distortion (right panels); namely, a fan of LLs that split into two, with overall larger splittings obtained for larger values of the finite parameter. Some of these splittings are indicated in Fig. 6(h). However, we have found that the ε_F -dependence of these splittings are distinct for the cases of ($\lambda_\sigma \neq 0, \Delta = 0$) and ($\lambda_\sigma = 0, \Delta \neq 0$).

Figure 7 shows the LL magnetic-field splittings of the bottom three split pairs indicated in Fig. 6(h), as functions of the Fermi energy, setting $\lambda_\sigma = 0$. Figure 7(a), shows that, for a pure Kek-Y distortion ($\lambda_\sigma = 0$), all three splittings exhibit a power-law behavior

$$\delta B_\rho(\varepsilon_F) = A_\rho \varepsilon_F^2, \quad (22)$$

where $\rho = \blacksquare, \blacktriangle, \blacklozenge$ indicates the corresponding magnetic field splitting shown in Fig. 6. For instance, for the rightmost splitting one can analytically compute the coefficient (see Appendix D)

$$A_{\blacksquare} = \frac{8\Delta^2}{\hbar^2 v_F^2} \sqrt{\frac{c}{2e\hbar}}, \quad (23)$$

up to third order in Δ . By contrast, Fig. 7(b) shows that, in the case of pure RSO coupling ($\Delta = 0$), there is a clear saturation of the splitting energies at large ε_F , with the first LL splitting (symbol \blacksquare) showing saturation already for $\varepsilon_F \approx 50$ meV. The saturation value of the first LL splitting can be computed as (see Appendix D)

$$\delta B_{\blacksquare}(\varepsilon_F \gg \lambda_\sigma) = \frac{2\lambda_\sigma^2}{\hbar^2 v_\sigma^2} \sqrt{\frac{c}{2e\hbar}}. \quad (24)$$

We propose that these distinct behaviors may be used experimentally, not only to distinguish between the two effects, but also to estimate the magnitude of the Kekulé distortion or RSO coupling, using doping-dependent magnetotransport measurements.

Figure 7(c) shows the predicted magnetic field splittings for a graphene sample with both a Kek-Y distortion, and a finite RSO coupling, the latter without a Kekulé modulation ($\xi = 0$). Although the analysis that led us to Eqs. (23) and (24) can be repeated in this case, the resulting expressions are much more complicated and far less illuminating. Nonetheless, the simultaneous presence of both the Kek-Y distortion and the Rashba effect can be inferred from the first (\blacksquare) splitting: Figure 7(c) shows

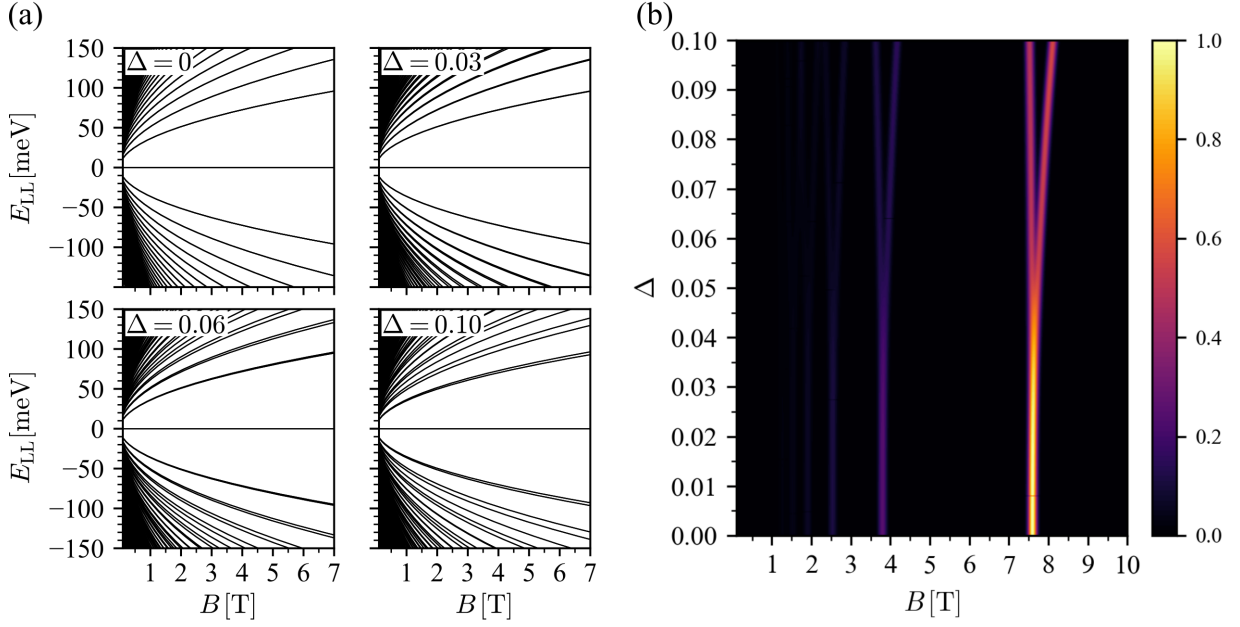


FIG. 5. (a) Landau levels for different values of Δ , and (b) $B^2 \cdot \text{DOS}(\varepsilon_F)$ (arbitrary units) as a function of Δ and magnetic field, for $\lambda_\sigma = \xi = 0$. In panel (b) we have set $\varepsilon_F = 50$ meV.

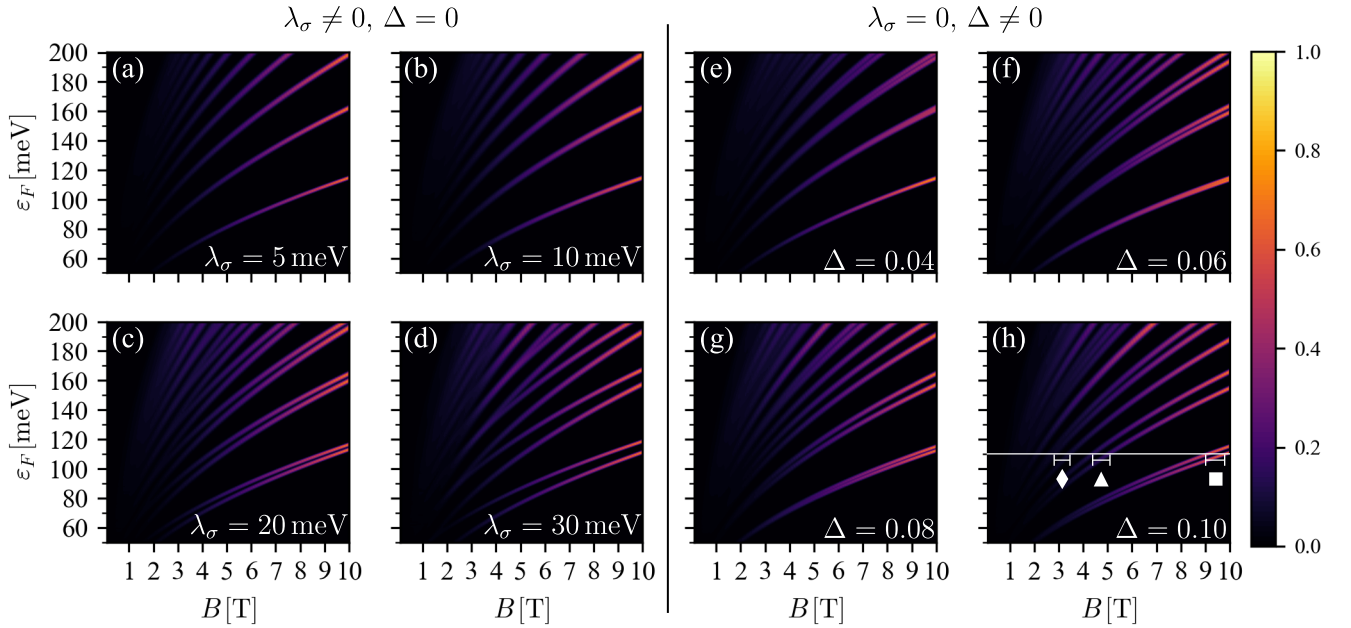


FIG. 6. $B^2 \cdot \text{DOS}(\varepsilon_F)$ as a function of the Fermi energy ε_F and magnetic field B , for $\xi = 0$. Left (right) panels correspond to model (17) with $\Delta = 0$ ($\Delta \neq 0$). The markers in panel (h) indicate the splittings described in Fig. 7.

a crossover from a saturating behavior at low ε_F , consistent with $\lambda_\sigma \neq 0$, to a monotonic increase at large ε_F when the Kek-Y distortion begins to dominate. Importantly, note that the initial plateau that appears before the crossover exceeds the theoretical value for the case of only RSO coupling (24), shown by the cyan line in Fig. 7(c). Therefore, when aiming to determine the values

of the Hamiltonian parameters λ_σ and Δ from magnetotransport experiments, it is important to explore beyond the weak doping regime, to avoid overestimating the value of λ_σ .

Finally, we briefly discuss the case where all Kek-Y model parameters λ_σ , Δ and ξ are finite. The corresponding LL spectrum is shown in Fig. 8 of Appendix

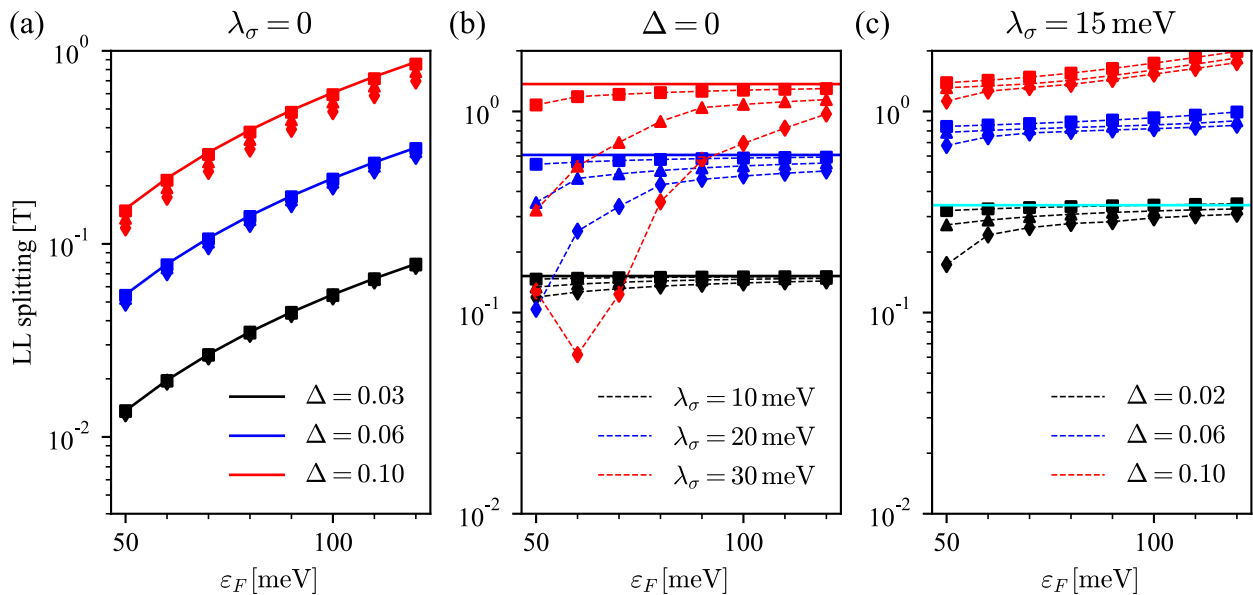


FIG. 7. Energy splittings of the lower three LL pairs as functions of the Fermi energy ε_F , for fixed model parameters (a) ($\lambda_\sigma = 0, \Delta \neq 0$), (b) ($\lambda_\sigma \neq 0, \Delta = 0$) and (c) ($\lambda_\sigma \neq 0, \Delta \neq 0$), with $\xi = 0$ in all cases. The data symbols (\blacksquare , \blacktriangle and \blacklozenge) are matched to those shown in Fig. 6(h). The solid lines in panel (a) correspond to Eq. (22) with the coefficient A_{\blacksquare} given by Eq. (23), whereas in panel (b) the solid lines indicate the saturation value given by Eq. (24). The cyan solid line in panel (c) indicates the saturation value predicted by Eq. (24), which is exceeded in the presence of a Kek-Y distortion. The dashed lines in panels (b) and (c) are merely guides to the eye.

C. In this case, the LL structure is quite complex, and a doping-dependent magnetic-field-splitting analysis becomes intractable. However, the new dispersion has a salient feature that is absent when either $\Delta = 0$ or $\lambda_\sigma = 0$; namely, that the zero-energy quadruplet shown in Figs. 4(a) and 5(a) splits for finite magnetic fields into a zero-energy doublet, closely surrounded by two electron-hole symmetric LLs. For small values of $|\Delta - \xi|$, the splitting between the latter two LLs takes the form ($v_\sigma(B) \equiv v_\sigma \sqrt{\frac{2e\hbar B}{c}}$, see Appendix B)

$$\delta\varepsilon_{z'} = \frac{2\lambda_\sigma v_\sigma(B)}{\sqrt{(1 + \Delta^2)v_\sigma^2(B) + (1 + \xi^2)\lambda_\sigma^2}} |\Delta - \xi|, \quad (25)$$

and is always finite, with the exception of the fine-tuned case $\Delta = \xi$. It is possible that this feature may be observed in magnetotransport experiments at very low doping levels, thus confirming that both a Kek-Y texture and a finite RSO coupling are present in the graphene system the presence of a Kekulé-induced modulation of the RSO coupling in Kek-Y graphene. Moreover, if the parameters Δ and λ_σ are estimated from the previously discussed analysis of the magnetic-field splittings, they may be introduced into Eq. (25), thus allowing for a rough estimation of the RSO modulation parameter ξ .

IV. CONCLUSIONS

We have introduced generalized tight-binding Hamiltonians for graphene with Kekulé-Y and Kekulé-O bond

textures, as well as Rashba spin-orbit coupling, which takes into account a possible modulation of the Rashba term by the Kekulé bond distortions. These models aim to describe epitaxial Kekulé graphene on transition metal surfaces, which have been shown to induce sizable Rashba spin-orbit couplings through proximity effects. We have also derived low-energy effective models based on the general tight-binding Hamiltonians, following the scheme introduced by Gamayun *et al.*[1]. We have found that, whereas the Kekulé-O effective model is independent of the Rashba term modulation, the Kekulé-Y model exhibits a new spin-valley locking term that can dramatically modify the Fermi surface of the system in charge neutrality.

We have also studied the Landau level spectrum of this system under a perpendicular magnetic field, and computed its density of states at the Fermi level with an aim to motivate magnetotransport experiments on Kekulé graphene systems on transition metal substrates. We have found that, whereas the Landau level spectra exhibit a degenerate quadruplet of zero-energy modes in graphene with either a Kekulé-Y distortion or Rashba spin-orbit coupling, this degeneracy is partially lifted when both effects are present, resulting on a degenerate doublet of zero-energy modes closely surrounded by two satellite Landau levels. Based on our findings, we have put forth an experimental method to distinguish the presence of the Kekulé-Y bond texture, of a Rashba spin-orbit term, or both, based on an analysis of the magnetic-field splittings of the DOS peaks, as functions of the Fermi energy. Finally, we have shown that, once the strengths

of both effects are extracted from this analysis, they may be used to estimate the magnitude of the Kekulé-induced modulation of the Rashba spin-orbit coupling based on the magnitude of the zero-energy mode splitting, which may be experimentally resolved at low enough values of the Fermi energy.

ACKNOWLEDGMENTS

D.A.R.T. acknowledges funding from PAPIIT-DGAPA-UNAM through project IA106523. F.M. acknowledges funding from PAPIIT-DGAPA-UNAM through project IN113920.

Appendix A: Effective low-energy Bloch Hamiltonians

Starting from Eq. (12), we identify the four high-energy bands corresponding to states at the Γ point of the original BZ, and neglect them, which corresponds

$$\Lambda_0^{\mu\nu}(\mathbf{k}) = \frac{\lambda_\sigma}{3} e^{ia_0k_y} \left[1 + 2 \cos \left(\frac{\sqrt{3}}{2} a_0 k_x + \frac{2\pi}{3} \gamma_{\mu\nu} \right) e^{-i\frac{3}{2} a_0 k_y} \right], \quad (\text{A3a})$$

$$\Lambda_{\pm 1}^{\mu\nu}(\mathbf{k}) = \frac{\lambda_\sigma}{6} e^{-ia_0k_y} \left[(1 \mp 3) \cos \left(\frac{\sqrt{3}}{2} a_0 k_x \right) + \sqrt{3} (\gamma_{\mu\nu} \pm 1) \sin \left(\frac{\sqrt{3}}{2} a_0 k_x \right) + 2e^{ia_0k_y} \right], \quad (\text{A3b})$$

where we have defined $\gamma_{\uparrow\downarrow} = -\gamma_{\downarrow\uparrow} = 1$. Moreover, $\Lambda_n^{\mu\mu}(\mathbf{k}) = 0$.

We now focus on momenta close to the KBZ Γ point, and expand all expressions up to first order in $a_0\mathbf{k}$ to obtain ($\hbar v_\sigma = \frac{3}{2} a_0 t_0$)

$$\Phi_0(\mathbf{k}) \approx -3t_0, \quad (\text{A4a})$$

$$\Phi_{\pm 1}(\mathbf{k}) \approx \hbar v_\sigma (\mp k_x + ik_y), \quad (\text{A4b})$$

$$\Lambda_0^{\uparrow\downarrow}(\mathbf{k}) = - \left(\Lambda_0^{\downarrow\uparrow}(\mathbf{k}) \right)^* \approx -\frac{\lambda_\sigma}{2} a_0 (k_x - ik_y), \quad (\text{A4c})$$

$$\Lambda_1^{\uparrow\downarrow}(\mathbf{k}) = - \left(\Lambda_{-1}^{\downarrow\uparrow}(\mathbf{k}) \right)^* \approx \frac{\lambda_\sigma}{2} a_0 (k_x + ik_y), \quad (\text{A4d})$$

$$\Lambda_{-1}^{\uparrow\downarrow}(\mathbf{k}) = \Lambda_1^{\downarrow\uparrow}(\mathbf{k}) \approx \lambda_\sigma. \quad (\text{A4e})$$

For clarity, we now use the basis ordering chosen in Ref. [1] for each spin quantum number, $\psi'_{\mathbf{k}} = (\psi'_{\mathbf{k},\uparrow}, \psi'_{\mathbf{k},\downarrow})^T$, with ($s = \uparrow, \downarrow$)

$$\psi_{\mathbf{k},s} = (-b_{\mathbf{k}-\mathbf{G},s}, a_{\mathbf{k}-\mathbf{G},s}, a_{\mathbf{k}+\mathbf{G},s}, b_{\mathbf{k}+\mathbf{G},s})^T,$$

to projecting them out at zeroth order in perturbation theory. This is justified by the large offset between these states and the Fermi level ($\approx 3\text{eV}$), as compared with all relevant model parameters, which fall in the 10 meV range. Collecting the annihilation operators in the column vector $\psi_{\mathbf{k}} = (a_{\mathbf{k}-\mathbf{G},\uparrow}, a_{\mathbf{k}-\mathbf{G},\downarrow}, a_{\mathbf{k}+\mathbf{G},\uparrow}, a_{\mathbf{k}+\mathbf{G},\downarrow}, b_{\mathbf{k}-\mathbf{G},\uparrow}, b_{\mathbf{k}-\mathbf{G},\downarrow}, b_{\mathbf{k}+\mathbf{G},\uparrow}, b_{\mathbf{k}+\mathbf{G},\downarrow})^T$, we write the total Hamiltonian for the eight bands closest to the Fermi level as

$$\mathcal{H}'_{pq}(\mathbf{k}) = \begin{pmatrix} 0 & \Sigma_n(\mathbf{k}) \\ \Sigma_n^\dagger(\mathbf{k}) & 0 \end{pmatrix}, \quad (\text{A1})$$

with n given by the Kekulé texture parameters p and q through Eq. (5), and

$$\Sigma_n(\mathbf{k}) = \begin{pmatrix} \Phi_{-1}(\mathbf{k}) & i\Lambda_{-1}^{\uparrow\downarrow}(\mathbf{k}) & \Delta\Phi_n(\mathbf{k}) & i\xi\Lambda_n^{\uparrow\downarrow}(\mathbf{k}) \\ i\Lambda_{-1}^{\downarrow\uparrow}(\mathbf{k}) & \Phi_{-1}(\mathbf{k}) & i\xi\Lambda_n^{\downarrow\uparrow}(\mathbf{k}) & \Delta\Phi_n(\mathbf{k}) \\ \Delta^*\Phi_{-n}(\mathbf{k}) & i\xi^*\Lambda_{-n}^{\uparrow\downarrow}(\mathbf{k}) & \Phi_1(\mathbf{k}) & i\Lambda_1^{\uparrow\downarrow}(\mathbf{k}) \\ i\xi^*\Lambda_{-n}^{\downarrow\uparrow}(\mathbf{k}) & \Delta^*\Phi_n(\mathbf{k}) & i\Lambda_1^{\downarrow\uparrow}(\mathbf{k}) & \Phi_1(\mathbf{k}) \end{pmatrix}. \quad (\text{A2})$$

where $\Phi_n(\mathbf{k}) = \Phi_n(\mathbf{k} + n\mathbf{G})$ and $\Lambda_n^{\mu\nu}(\mathbf{k}) = \Lambda_{\mu\nu}(\mathbf{k} + n\mathbf{G})$, following the definitions (9). For $\mu \neq \nu$ we obtain explicitly

such that the effective Hamiltonian adopts the form

$$\mathcal{H}''_{pq}(\mathbf{k}) = \begin{pmatrix} \mathcal{H}_0^{pq}(\mathbf{k}) & 0_{4 \times 4} \\ 0_{4 \times 4} & \mathcal{H}_0^{pq}(\mathbf{k}) \end{pmatrix} + \begin{pmatrix} 0_{4 \times 4} & \mathcal{H}_R^{pq}(\mathbf{k}) \\ \mathcal{H}_R^{pq\dagger}(\mathbf{k}) & 0_{4 \times 4} \end{pmatrix} \quad (\text{A5})$$

where

$$\mathcal{H}_0^{pq}(\mathbf{k}) = \begin{pmatrix} \hbar v_\sigma \mathbf{k} \cdot \boldsymbol{\sigma} & \Delta Q_n(\mathbf{k}) \\ \Delta^* Q_n^\dagger(\mathbf{k}) & \hbar v_\sigma \mathbf{k} \cdot \boldsymbol{\sigma} \end{pmatrix} \quad (\text{A6})$$

is the usual Kekulé graphene Hamiltonian for either a Kek-O ($Q_0 = 3t_0\sigma_z$) or a Kek-Y [$Q_{\pm 1} = \hbar v_\sigma (\pm k_x - ik_y)\sigma_0$] texture. The Kekulé-RSO term $\mathcal{H}_R^{pq}(\mathbf{k})$ has the general form

$$\mathcal{H}_R^{pq}(\mathbf{k}) = \begin{pmatrix} 0 & i(\Delta_{-1}^{\downarrow\uparrow}(\mathbf{k}))^* & i\xi(\Delta_{-n}^{\downarrow\uparrow}(\mathbf{k}))^* & 0 \\ -i\Delta_{-1}^{\uparrow\downarrow}(\mathbf{k}) & 0 & 0 & i\xi\Delta_n^{\uparrow\downarrow}(\mathbf{k}) \\ -i\xi^*\Delta_{-n}^{\uparrow\downarrow}(\mathbf{k}) & 0 & 0 & i\Delta_1^{\uparrow\downarrow}(\mathbf{k}) \\ 0 & -i\xi^*(\Delta_n^{\downarrow\uparrow}(\mathbf{k}))^* & -i(\Delta_1^{\downarrow\uparrow}(\mathbf{k}))^* & 0 \end{pmatrix},$$

and simplifies as follows for the three possible values $n = -1, 0, 1$: For $n = 0$ we get the Kek-O effective model

$$\mathcal{H}_R^{n=0}(\mathbf{k}) = \begin{pmatrix} 0 & -i\frac{\lambda_\sigma}{2}a_0(k_x + ik_y) & i\xi\frac{\lambda_\sigma}{2}a_0(k_x - ik_y) & 0 \\ -i\lambda_\sigma & 0 & 0 & -i\xi\frac{\lambda_\sigma}{2}a_0(k_x - ik_y) \\ i\xi^*\frac{\lambda_\sigma}{2}a_0(k_x - ik_y) & 0 & 0 & i\frac{\lambda_\sigma}{2}a_0(k_x + ik_y) \\ 0 & -i\xi^*\frac{\lambda_\sigma}{2}a_0(k_x - ik_y) & -i\lambda_\sigma & 0 \end{pmatrix}, \quad (\text{A7})$$

whereas for $n = \pm 1$ we obtain the Kek-Y effective models

$$\mathcal{H}_R^{n=1}(\mathbf{k}) = \begin{pmatrix} 0 & -i\frac{\lambda_\sigma}{2}a_0(k_x + ik_y) & -i\xi\frac{\lambda_\sigma}{2}a_0(k_x + ik_y) & 0 \\ -i\lambda_\sigma & 0 & 0 & i\xi\frac{\lambda_\sigma}{2}a_0(k_x + ik_y) \\ -i\xi^*\lambda_\sigma & 0 & 0 & i\frac{\lambda_\sigma}{2}a_0(k_x + ik_y) \\ 0 & -i\xi^*\lambda_\sigma & -i\lambda_\sigma & 0 \end{pmatrix}, \quad (\text{A8a})$$

$$\mathcal{H}_R^{n=-1}(\mathbf{k}) = \begin{pmatrix} 0 & -i\frac{\lambda_\sigma}{2}a_0(k_x + ik_y) & i\xi\lambda_\sigma & 0 \\ -i\lambda_\sigma & 0 & 0 & i\xi\lambda_\sigma \\ -i\xi^*\frac{\lambda_\sigma}{2}a_0(k_x + ik_y) & 0 & 0 & i\frac{\lambda_\sigma}{2}a_0(k_x + ik_y) \\ 0 & i\xi^*\frac{\lambda_\sigma}{2}a_0(k_x + ik_y) & -i\lambda_\sigma & 0 \end{pmatrix}. \quad (\text{A8b})$$

Equations (17) and (18) are obtained from Eqs. (A8) and (A7), respectively, by reordering the basis according to Eq. (16), and neglecting the terms linear in momentum.

Appendix B: Landau levels Hamiltonian for the Kek-Y case

For the Kekulé-Y case, the electronic Hamiltonian is obtained from (17) by substituting[35, 36]

$$\begin{aligned} \hbar v_\sigma(k_x + ik_y) &\longrightarrow v_\sigma(B)a^\dagger, \\ \hbar v_\sigma(k_x - ik_y) &\longrightarrow v_\sigma(B)a, \end{aligned}$$

with $v_\sigma(B) \equiv v_\sigma\sqrt{\frac{2e\hbar B}{c}}$ (in Gaussian units), and a and a^\dagger the LL ladder operators. Ordering the basis as

$$\{|\uparrow, 1, -1\rangle, |\uparrow, -1, 1\rangle, |\downarrow, 1, -1\rangle, |\downarrow, -1, 1\rangle, |\uparrow, -1, -1\rangle, |\uparrow, 1, 1\rangle, |\downarrow, -1, -1\rangle, |\downarrow, 1, 1\rangle\}$$

where the quantum numbers correspond to spin (s), pseudo-spin (σ) and valley (τ), respectively, the Landau level Hamiltonian takes the form

$$H_{\mathcal{KY}}^{LL} = \begin{pmatrix} 0 & h(B) \\ h^\dagger(B) & 0 \end{pmatrix}, \quad (\text{B1})$$

$$h_\ell(B) = \begin{pmatrix} v_\sigma(B)\sqrt{\ell-1} & \Delta v_\sigma(B)\sqrt{\ell-2} & 0 & -i\xi\lambda_\sigma \\ \Delta v_\sigma(B)\sqrt{\ell-1} & v_\sigma(B)\sqrt{\ell-2} & 0 & -i\lambda_\sigma \\ i\lambda_\sigma & 0 & v_\sigma(B)\sqrt{\ell} & \Delta v_\sigma(B)\sqrt{\ell-1} \\ i\xi\lambda_\sigma & 0 & \Delta v_\sigma(B)\sqrt{\ell} & v_\sigma(B)\sqrt{\ell-1} \end{pmatrix}, \quad \ell \geq 3. \quad (\text{B5})$$

Setting $\ell = 2$ yields the reduced problem

$$H_{\mathcal{KY}}^{LL}|\psi_2\rangle = \begin{pmatrix} 0_{4\times 4} & h_2(B) \\ h_2^\dagger(B) & 0_{3\times 3} \end{pmatrix}|\psi_2\rangle, \quad (\text{B6})$$

with

$$h(B) = \begin{pmatrix} v_\sigma(B)a & \Delta v_\sigma(B)a^\dagger & 0 & -i\xi\lambda_\sigma \\ \Delta v_\sigma(B)a & v_\sigma(B)a^\dagger & 0 & -i\lambda_\sigma \\ i\lambda_\sigma & 0 & v_\sigma(B)a & \Delta v_\sigma(B)a^\dagger \\ i\xi\lambda_\sigma & 0 & \Delta v_\sigma(B)a & v_\sigma(B)a^\dagger \end{pmatrix}. \quad (\text{B2})$$

Defining the Landau level eigenstates $|s, \sigma, \tau; \ell\rangle$ ($\ell = 0, 1, 2, \dots$), we may propose a general solution of the form

$$|\psi_\ell\rangle = \begin{pmatrix} |\ell-2\rangle \\ |\ell-2\rangle \\ |\ell-1\rangle \\ |\ell-1\rangle \\ |\ell-1\rangle \\ |\ell-3\rangle \\ |\ell\rangle \\ |\ell-2\rangle \end{pmatrix}, \quad (\text{B3})$$

such that for $\ell \geq 3$ we get

$$H_{\mathcal{KY}}^{LL}|\psi_\ell\rangle = \begin{pmatrix} 0_{4\times 4} & h_n(B) \\ h_n^\dagger(B) & 0_{4\times 4} \end{pmatrix}|\psi_\ell\rangle, \quad (\text{B4})$$

with

$$h_2(B) = \begin{pmatrix} v_\sigma(B) & 0 & -i\xi\lambda_\sigma \\ \Delta v_\sigma(B) & 0 & -i\lambda_\sigma \\ i\lambda_\sigma & \sqrt{2}v_\sigma(B) & \Delta v_\sigma(B) \\ i\xi\lambda_\sigma & \sqrt{2}\Delta v_\sigma(B) & v_\sigma(B) \end{pmatrix} \quad (\text{B7})$$

and the reduced basis

$$\{|\uparrow, 1, -1; 0\rangle, |\uparrow, -1, 1; 0\rangle, |\downarrow, 1, -1; 1\rangle, |\downarrow, -1, 1; 1\rangle, |\uparrow, -1, -1; 1\rangle, |\downarrow, -1, -1; 2\rangle, |\downarrow, 1, 1; 0\rangle\} \quad (\text{B8})$$

From this case we can extract the valley-sublattice-locked ($\tau\sigma = -1$) zero-energy mode

$$|z_-\rangle = N_z^{-\frac{1}{2}} \left[-(\Delta\alpha - \beta)|\uparrow, 1, -1; 0\rangle + (\alpha - \xi\beta)|\uparrow, -1, 1; 0\rangle + i\Delta\gamma|\downarrow, 1, -1; 1\rangle - i\gamma|\downarrow, -1, 1; 1\rangle \right], \quad (\text{B9})$$

where

$$\alpha = v_\sigma^2(B)(1 - \Delta^2), \quad (\text{B10a})$$

$$\beta = \lambda_\sigma^2(\xi - \Delta), \quad (\text{B10b})$$

$$\gamma = \lambda_\sigma v_\sigma(B)\Delta(1 - \xi\Delta), \quad (\text{B10c})$$

$$N_z = (\alpha^2 + \gamma^2)(1 + \Delta^2) + \beta^2(1 + \xi^2) - 2(\xi + \Delta)\alpha\beta. \quad (\text{B10d})$$

Then, setting $\ell = 1$ we obtain the reduced problem

$$H_{\text{KekY}}^{LL}|\psi_1\rangle = \begin{pmatrix} 0_{2 \times 2} & h_1(B) \\ h_1^\dagger(B) & 0_{2 \times 2} \end{pmatrix} |\psi_1\rangle, \quad (\text{B11})$$

with

$$h_1(B) = \begin{pmatrix} i\lambda_\sigma & v_\sigma(B) \\ i\xi\lambda_\sigma & \Delta v_\sigma(B) \end{pmatrix}, \quad (\text{B12})$$

and the reduced basis

$$\{|\downarrow, 1, -1; 0\rangle, |\downarrow, -1, 1; 0\rangle, |\uparrow, -1, -1; 0\rangle, |\downarrow, -1, -1; 1\rangle\}.$$

This can be diagonalized analytically, and gives the eigenvalues ($\eta, \zeta = \pm 1$)

$$\varepsilon_{\eta, \zeta}(B) = \frac{\eta}{\sqrt{2}} \sqrt{(1 + \Delta^2)v_\sigma^2(B) + (1 + \xi^2)\lambda_\sigma^2 + \zeta \sqrt{[(1 + \Delta^2)v_\sigma^2(B) + (1 + \xi^2)\lambda_\sigma^2]^2 - 4\lambda_\sigma^2 v_\sigma^2(B)(\Delta - \xi)^2}}. \quad (\text{B13})$$

Two additional zero modes are recovered in the case of $\xi = \Delta$, corresponding to the eigenstates

$$|z'_+\rangle = \frac{v_\sigma(B)|\uparrow, -1, -1; 1\rangle - i\lambda_\sigma|\downarrow, -1, -1; 0\rangle}{\sqrt{v_\sigma^2(B) + \lambda_\sigma^2}},$$

$$|z'_-\rangle = \frac{-\Delta|\downarrow, 1, -1; 0\rangle + |\downarrow, -1, 1; 1\rangle}{\sqrt{1 + \Delta^2}},$$

which split as

$$\delta\varepsilon_{z'} = \frac{2\lambda_\sigma v_\sigma(B)}{\sqrt{(1 + \Delta^2)v_\sigma^2(B) + (1 + \xi^2)\lambda_\sigma^2}} |\Delta - \xi| \quad (\text{B14})$$

for $0 < |\Delta - \xi| \ll 1$.

Finally, setting $\ell = 0$ yields the zero-energy mode

$$|z_+\rangle = |\downarrow, -1, -1; 0\rangle. \quad (\text{B15})$$

Note that in the absence of Rashba spin-orbit coupling ($\lambda_\sigma \rightarrow 0$), the four zero-energy modes identified reduce

to those reported by Gamayun *et al.* in Ref. 1:

$$|z_+\rangle|_{\lambda_\sigma=0} = |\downarrow, -1, -1; 0\rangle,$$

$$|z'_+\rangle|_{\lambda_\sigma=0} = |\uparrow, -1, -1; 1\rangle,$$

$$|z_-\rangle|_{\lambda_\sigma=0} = \frac{-\Delta|\uparrow, 1, -1; 0\rangle + |\uparrow, -1, 1; 0\rangle}{\sqrt{1 + \Delta^2}},$$

$$|z'_-\rangle|_{\lambda_\sigma=0} = \frac{-\Delta|\downarrow, 1, -1; 0\rangle + |\downarrow, -1, 1; 1\rangle}{\sqrt{1 + \Delta^2}}.$$

Appendix C: Landau level spectrum of Kek-Y graphene with RSO coupling

Figure 8 shows the LL spectra of Kek-Y graphene, with fixed Kekulé parameter $\Delta = 0.1$, and for several values of the RSO term λ_σ , keeping the RSO distortion $\xi = 0$. At first sight, this LL spectrum resembles that of RSO graphene (Fig. 4), with a duplicated fan due to the two Fermi velocities introduced by the Kek-Y distortion (Fig. 5). However, a major qualitative difference with those cases is that the zero-energy quadruplet breaks into a zero-energy doublet surrounded by two dispersive LLs that split according to Eq. (B14).

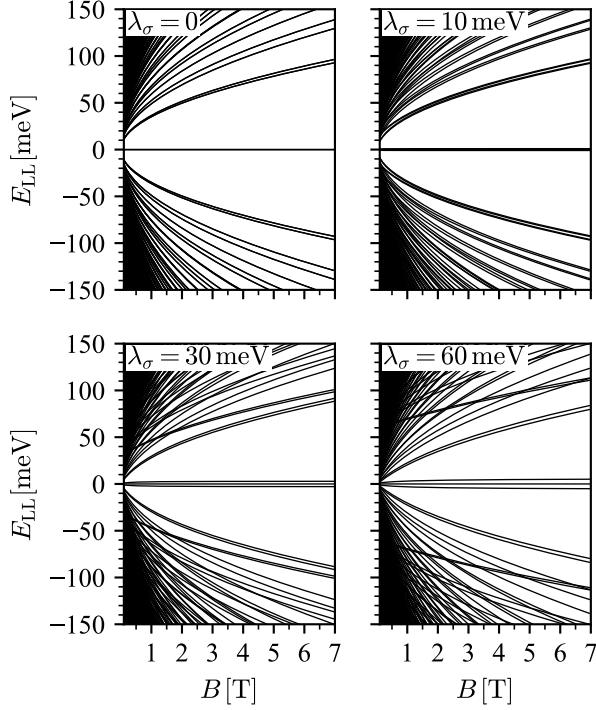


FIG. 8. Landau levels for different values of λ_σ , keeping $\Delta = 0.1$ fixed. Note the splitting of the zero-energy quadruplet for $\lambda_\sigma \neq 0$, into a zero-energy doublet and two dispersive LLs.

Appendix D: Magnetic field splittings in the Fermi-level dependent DOS of pure Kek-Y and RSO samples

The high-DOS fans in Fig. 7 are direct visualizations of constant energy cuts of the LL fans of Figs. 4 and 5, for $E_{LL} = \varepsilon_F$. The ε_F -dependent splittings can be extracted directly from the B -dependent eigenvalues of the LL Hamiltonians (B4), (B6) and (B11). For simplicity, let us focus on the splitting between the rightmost splitting, indicated in Fig. 7(h) with the symbol ■.

In the case of only a Kek-Y distortion ($\Delta \neq 0$, $\lambda_\sigma = 0$, $\xi = 0$), this splitting occurs between the LLs

$$\begin{aligned} \varepsilon_4^{(1)}(B) &= v_\sigma(B) \sqrt{1 + \Delta^2}, \\ \varepsilon_5^{(2)}(B) &= v_\sigma(B) \sqrt{\frac{3(1 + \Delta^2) - \sqrt{1 + 34\Delta^2 + \Delta^4}}{2}}, \end{aligned} \quad (\text{D1})$$

where $\varepsilon_m^{(\ell)}$ is the m th eigenvalue, by increasing energy, obtained from the model (B4) by fixing the LL index ℓ . The magnetic field splitting between these two LLs at fixed ε_F is obtained as $\delta B = B_> - B_<$, where

$$\varepsilon_5^{(2)}(B_>) = \varepsilon_4^{(1)}(B_<) = \varepsilon_F. \quad (\text{D2})$$

This gives

$$\begin{aligned} \delta B &= \frac{\varepsilon_F^2}{\hbar^2 v_\sigma^2} \sqrt{\frac{c}{2e\hbar}} \\ &\times \left[\frac{2}{3(1 + \Delta^2) - \sqrt{1 + 34\Delta^2 + \Delta^4}} - \frac{1}{1 + \Delta^2} \right] \\ &= \frac{8\Delta^2}{\hbar^2 v_\sigma^2} \varepsilon_F^2 \sqrt{\frac{c}{2e\hbar}} + \mathcal{O}\{\Delta^4\}, \end{aligned} \quad (\text{D3})$$

leading to Eqs. (22) and (23).

We may follow the same procedure in the case of only RSO coupling ($\Delta = 0$, $\lambda_\sigma \neq 0$, $\xi = 0$), where the relevant LL energies are

$$\begin{aligned} \varepsilon_4^{(1)}(B) &= \sqrt{\hbar^2 v_\sigma^2(B) + \lambda_\sigma^2}, \\ \varepsilon_5^{(2)}(B) &= \sqrt{\frac{3v_\sigma^2(B) + \lambda_\sigma^2 - \sqrt{v_\sigma^4(B) + 6\lambda_\sigma^2 v_\sigma^2(B) + \lambda_\sigma^4}}{2}}. \end{aligned} \quad (\text{D4})$$

In this case, Eq. (D2) gives $B_< = \frac{\varepsilon_F^2 - \lambda_\sigma^2}{\hbar^2 v_\sigma^2} \sqrt{\frac{c}{2e\hbar}}$, whereas for $B_>$ we get the equation

$$\begin{aligned} 2\varepsilon_F^2 &= \lambda_\sigma^2 + (\hbar v_\sigma)^2 \sqrt{\frac{c}{2e\hbar}} B \\ &\times \left[3 - \sqrt{1 + \frac{6\lambda_\sigma^2}{(\hbar v_\sigma)^2 B} \sqrt{\frac{c}{2e\hbar}} + \frac{\lambda_\sigma^4}{(\hbar v_\sigma)^4 B^2} \frac{c}{2e\hbar}} \right]. \end{aligned}$$

This can be simplified by working in the limit of $\frac{\lambda_\sigma^2}{v_\sigma^2(B)} \ll 1$, and expanding up to second order. This gives the quadratic equation

$$B^2 - \frac{\varepsilon_F^2 + \lambda_\sigma^2}{\hbar^2 v_\sigma^2} \sqrt{\frac{c}{2e\hbar}} B + \frac{2\lambda_\sigma^4}{\hbar^2 v_\sigma^4} \frac{c}{2e\hbar} \approx 0,$$

from which we take the solution

$$B_> \approx \frac{\varepsilon_F^2 + \lambda_\sigma^2}{2\hbar^2 v_\sigma^2} \left[1 + \sqrt{1 - \frac{8\lambda_\sigma^4}{(\varepsilon_F^2 + \lambda_\sigma^2)^2}} \right].$$

In the limit of $\frac{\lambda_\sigma}{\varepsilon_F} \ll 1$ we may approximate $B_> \approx \frac{\varepsilon_F^2 + \lambda_\sigma^2}{2\hbar^2 v_\sigma^2}$, yielding the magnetic field splitting

$$\delta B = \frac{2\lambda_\sigma^2}{\hbar^2 v_\sigma^2} \sqrt{\frac{c}{2e\hbar}} + \mathcal{O}\left\{\left(\frac{\lambda_\sigma}{\varepsilon_F}\right)^2\right\}, \quad (\text{D5})$$

leading to Eq. (24).

- [1] O V Gamayun, V P Ostroukh, N V Gnezdilov, Í Adagideli, and C W J Beenakker. Valley-momentum locking in a graphene superlattice with y-shaped kekulé bond texture. *New Journal of Physics*, 20(2):023016, 2018.
- [2] Elena Voloshina and Yuriy Dedkov. Graphene on metallic surfaces: problems and perspectives. *Phys. Chem. Chem. Phys.*, 14:13502–13514, 2012.
- [3] P. A. Khomyakov, G. Giovannetti, P. C. Rusu, G. Brocks, J. van den Brink, and P. J. Kelly. First-principles study of the interaction and charge transfer between graphene and metals. *Phys. Rev. B*, 79:195425, May 2009.
- [4] G. Giovannetti, P. A. Khomyakov, G. Brocks, V. M. Karpan, J. van den Brink, and P. J. Kelly. Doping graphene with metal contacts. *Phys. Rev. Lett.*, 101:026803, Jul 2008.
- [5] Guibin Song, Mojtaba Ranjbar, David R. Daughton, and Richard A. Kiehl. Nanoparticle-Induced Anomalous Hall Effect in Graphene. *Nano Letters*, 19(10):7112–7118, 2019. PMID: 31513412.
- [6] C. K. Saefer, Josep Ingla-Aynés, Franz Herling, José H. Garcia, Marc Vila, Nerea Ontoso, M. Reyes Calvo, Stephan Roche, Luis E. Hueso, and Fèlix Casanova. Room-Temperature Spin Hall Effect in Graphene/MoS₂ van der Waals Heterostructures. *Nano Letters*, 19(2):1074–1082, 2019.
- [7] C. L. Kane and E. J. Mele. Quantum Spin Hall Effect in Graphene. *Phys. Rev. Lett.*, 95:226801, 2005.
- [8] A. Avsar, J. Y. Tan, T. Taychatanapat, J. Balakrishnan, G.K.W. Koon, Y. Yeo, J. Lahiri, A. Carvalho, A. S. Rodin, E.C.T. O’Farrell, G. Eda, A. H. Castro Neto, and B. Özyilmaz. Spin-orbit proximity effect in graphene. *Nature Communications*, 5, Sep 2014.
- [9] Wei Han, Roland K Kawakami, Martin Gmitra, and Jaroslav Fabian. Graphene spintronics. *Nature nanotechnology*, 9(10):794, 2014.
- [10] Zhuonan Lin, Wei Qin, Jiang Zeng, Wei Chen, Ping Cui, Jun-Hyung Cho, Zhenhua Qiao, and Zhenyu Zhang. Competing gap opening mechanisms of monolayer graphene and graphene nanoribbons on strong topological insulators. *Nano letters*, 17(7):4013–4018, 2017.
- [11] Daniel Huertas-Hernando, F. Guinea, and Arne Brataas. Spin-orbit coupling in curved graphene, fullerenes, nanotubes, and nanotube caps. *Phys. Rev. B*, 74:155426, Oct 2006.
- [12] L. González-Árraga, F. Guinea, and P. San-Jose. Modulation of kekulé adatom ordering due to strain in graphene. *Phys. Rev. B*, 97:165430, Apr 2018.
- [13] Alejandro López, Luis Colmenárez, Mayra Peralta, Francisco Mireles, and Ernesto Medina. Proximity-induced spin-orbit effects in graphene on au. *Phys. Rev. B*, 99:085411, Feb 2019.
- [14] Christopher Gutierrez, Cheol-Joo Kim, Lola Brown, Theanne Schiros, Dennis Nordlund, Edward B. Lochocki, Kyle M. Shen, Jiwoong Park, and Abhay N. Pasupathy. Imaging chiral symmetry breaking from kekulé bond order in graphene. *Nature Physics*, 12:950–958, 2016.
- [15] Christopher Gutierrez. *Visualizing Ordered Electronic States in Epitaxial Graphene*. PhD thesis, Columbia University, 2015.
- [16] Daejin Eom and Ja-Yong Koo. Direct measurement of strain-driven kekulé distortion in graphene and its electronic properties. *Nanoscale*, 12(38):19604–19608, 2020.
- [17] Si-Yu Li, Yu Zhang, Long-Jing Yin, and Lin He. Scanning tunneling microscope study of quantum hall isospin ferromagnetic states in the zero landau level in a graphene monolayer. *Phys. Rev. B*, 100:085437, Aug 2019.
- [18] Changhua Bao, Hongyun Zhang, Teng Zhang, Xi Wu, Laipeng Luo, Shaohua Zhou, Qian Li, Yanhui Hou, Wei Yao, Liwei Liu, Pu Yu, Jia Li, Wenhui Duan, Hong Yao, Yeliang Wang, and Shuyun Zhou. Experimental evidence of chiral symmetry breaking in kekulé-ordered graphene. *Phys. Rev. Lett.*, 126:206804, May 2021.
- [19] Changhua Bao, Hongyun Zhang, Xi Wu, Shaohua Zhou, Qian Li, Pu Yu, Jia Li, Wenhui Duan, and Shuyun Zhou. Coexistence of extended flat band and kekulé order in li-intercalated graphene. *Phys. Rev. B*, 105:L161106, Apr 2022.
- [20] AC Qu, P Nigge, S Link, G Levy, M Michiardi, PL Spandar, T Matthé, M Schneider, S Zhdanovich, U Starke, et al. Ubiquitous defect-induced density wave instability in monolayer graphene. *Science Advances*, 8(23):eabm5180, 2022.
- [21] D. Marchenko, A. Varykhalov, M.R. Scholz, G. Bihlmayer, E.I. Rashba, A. Rybkin, A.M. Shikin, and O. Rader. Giant Rashba splitting in graphene due to hybridization with gold. *Nature Communications*, 3:1232, November 2012.
- [22] A. Varykhalov, J. Sánchez-Barriga, A. M. Shikin, C. Biswas, E. Vescovo, A. Rybkin, D. Marchenko, and O. Rader. Electronic and magnetic properties of quasifreestanding graphene on ni. *Phys. Rev. Lett.*, 101:157601, Oct 2008.
- [23] Yu. S. Dedkov, M. Fonin, U. Rüdiger, and C. Laubschat. Rashba effect in the graphene/ni(111) system. *Phys. Rev. Lett.*, 100:107602, Mar 2008.
- [24] O. Rader, A. Varykhalov, J. Sánchez-Barriga, D. Marchenko, A. Rybkin, and A. M. Shikin. Is there a Rashba effect in graphene on 3d ferromagnets? *Phys. Rev. Lett.*, 102:057602, Feb 2009.
- [25] J. Sichau, M. Prada, T. Anlauf, T. J. Lyon, B. Bosnjak, L. Tiemann, and R. H. Blick. Resonance microwave measurements of an intrinsic spin-orbit coupling gap in graphene: A possible indication of a topological state. *Phys. Rev. Lett.*, 122:046403, Feb 2019.
- [26] Sergej Konschuh, Martin Gmitra, and Jaroslav Fabian. Tight-binding theory of the spin-orbit coupling in graphene. *Phys. Rev. B*, 82:245412, Dec 2010.
- [27] Mayra Peralta, Ernesto Medina, and Francisco Mireles. Proximity-induced exchange and spin-orbit effects in graphene on Ni and Co. *Phys. Rev. B*, 99:195452, May 2019.
- [28] B. Berche, F. Mireles, and E. Medina. Rashba spin-orbit interaction enhanced by graphene in-plane deformations. *Condens. Matter Phys*, 20(1), 2017.
- [29] J. M. Luttinger and W. Kohn. Motion of electrons and holes in perturbed periodic fields. *Phys. Rev.*, 97:869–883, Feb 1955.
- [30] C. L. Kane and E. J. Mele. Quantum spin Hall effect in graphene. *Phys. Rev. Lett.*, 95:226801, 2005.
- [31] C. L. Kane and E. J. Mele. Z_2 topological order and the quantum spin hall effect. *Phys. Rev. Lett.*, 95:146802,

- Sep 2005.
- [32] Emmanuel I. Rashba. Graphene with structure-induced spin-orbit coupling: Spin-polarized states, spin zero modes, and quantum hall effect. *Phys. Rev. B*, 79:161409, Apr 2009.
- [33] Yawar Mohammadi and Samira Bahrami. Integer quantum hall effect in kekulé-patterned graphene. *Chinese Physics B*, 31(1):017305, jan 2022.
- [34] JW McClure. Diamagnetism of graphite. *Phys. Rev*, 104(3):666, 1956.
- [35] J. M. Luttinger and W. Kohn. Motion of electrons and holes in perturbed periodic fields. *Phys. Rev.*, 97:869–883, Feb 1955.
- [36] Lev Davidovich Landau and Evgenii Mikhailovich Lifshitz. *Quantum mechanics: non-relativistic theory*, volume 3. Elsevier, 2013.